JOURNAL OF SPACECRAFT AND ROCKETS
Vol. 33, No. 1, January–February 1996

Base-Bleed Experiments with a Cylindrical Afterbody in Supersonic Flow

Tarun Mathur* and J. Craig Dutton†
University of Illinois at Urbana–Champaign, Urbana, Illinois 61801

The effect of base bleed on the near-wake flowfield of a cylindrical afterbody in a Mach 2.5 flow with a unit Reynolds number of 45×10^6 m^{-1} has been investigated. This study is aimed at better understanding the complex fluid-dynamic interactions occurring in the near wake due to base bleed and is motivated by the lack of detailed velocity and turbulence data in this flowfield. The experimental techniques used include static pressure measurements along the afterbody and the base plane, schlieren and shadowgraph photography, and centerline traverses in the near wake using two-component laser Doppler velocimetry. Results indicate relatively uniform radial pressure profiles across the base plane. With increasing bleed flow rate, the average base pressure is found to increase initially, attain a peak value near an injection parameter of $I = 0.0148$, and then decrease with further increase in I. The optimum bleed condition near $I = 0.0148$ is also characterized by a weak corner expansion, a minimum value of the free-shear-layer angle, and the near-disappearance of the recirculation region (reverse velocity) along the centerline of the near wake.

Nomenclature

A_b = base area, πR_0^2, m^2
C_f = skin-friction coefficient
H = compressible shape factor, δ^*/θ
I = dimensionless injection parameter, $\dot{m}_{\text{bleed}}/\rho_1 U_1 A_b$
k = turbulent kinetic energy, m^2/s^2
M = Mach number
$\dot{m}_{\text{bleed}}$ = bleed mass flow rate, kg/s
P = pressure, kPa
R_{jet} = bleed jet radius, mm
R_0 = afterbody radius, mm
r = radial coordinate, mm
T_0 = wind-tunnel stagnation temperature, K
U = mean axial velocity, m/s
U_1 = freestream approach velocity, m/s
u_τ = friction velocity, m/s
u' = instantaneous axial velocity fluctuation, m/s
v_r' = instantaneous radial velocity fluctuation, m/s
x = axial (streamwise) position relative to the base plane, mm
y = radial distance from sting surface, mm
δ = boundary-layer thickness, mm
δ^* = boundary-layer displacement thickness, mm
θ = boundary-layer momentum thickness, mm
ν_w = kinematic viscosity at the wall (sting surface) temperature, m^2/s
Π = boundary-layer wake strength parameter
ρ = density, kg/m^3
σ_U = axial rms velocity fluctuation, m/s
σ_{V_r} = radial rms velocity fluctuation, m/s
$\langle\ \rangle$ = ensemble-averaged value

Subscripts

b = base
0 = stagnation or afterbody
1 = freestream approach conditions

Introduction

FLOW separation at the base of aerodynamic vehicles such as missiles, rockets, and projectiles leads to the formation of a low-speed recirculation region near the base. The pressure in this region is generally significantly lower than the freestream pressure. Base drag, caused by this difference in pressures, can be up to two-thirds of the total drag on a body of revolution. Techniques such as boattailing, base burning, and base bleed have been used traditionally to reduce base drag; however, in the past, these techniques were applied in an empirical manner because of a lack of detailed data and understanding of the fluid-dynamic interactions occurring in the base region. With the advent of laser-based optical flow diagnostic techniques in the past decade, it is now possible to examine these flowfields in greater detail in a nonintrusive manner. Recently, a detailed investigation of supersonic axisymmetric base flows including the effects of afterbody boattailing was completed by Herrin and Dutton.[1,2] The research reported herein on base bleed is the logical extension of this recent investigation.

Figure 1 is a flowfield schematic of supersonic flow over a blunt, cylindrical body with base bleed. The supersonic freestream flow undergoes an expansion at the base corner as the turbulent approach boundary layer separates and forms a free shear layer. This shear layer eventually undergoes recompression, realignment, and redevelopment in the wake of the afterbody as it is constrained to turn along the axis of symmetry. The shear layer entrains fluid from the region behind the base and accelerates it. A recompression shock system returns this fluid to the base region, forming a recirculation region in the process. Injection of low-speed fluid into the base region displaces the forward stagnation point downstream of the base plane. The location of the forward stagnation point is determined by a balance between the momentum of the injected gas and that of the recirculating fluid. The magnitude of the bleed flow rate is quantified using a nondimensional injection parameter, I, defined as the bleed mass flow rate normalized by the product of the base area and the freestream mass flux. This definition of the injection parameter does not account for the approach boundary-layer thickness and the bleed flow momentum, both of which have been shown to affect the base pressure in a manner analogous to base bleed.

The effect of varying the bleed mass flow rate on the base pressure ratio, P_b/P_1, has been studied experimentally by several researchers.[3–7] The results of these experiments exhibit certain common trends and indicate three distinct operating regimes determined by the quantity of mass injected. The base pressure ratio increases fairly linearly with bleed rate at low values of I (regime 1). A peak in the base pressure ratio occurs at an intermediate value of I (near $I = 0.01$ for air), the value of which depends on several factors

---

Received Nov. 7, 1994; revision received April 27, 1995; accepted for publication April 28, 1995.

[*] Graduate Research Assistant, Department of Mechanical and Industrial Engineering, 1206 West Green Street. Student Member AIAA.

[†] Professor, Department of Mechanical and Industrial Engineering, 1206 West Green Street. Associate Fellow AIAA.

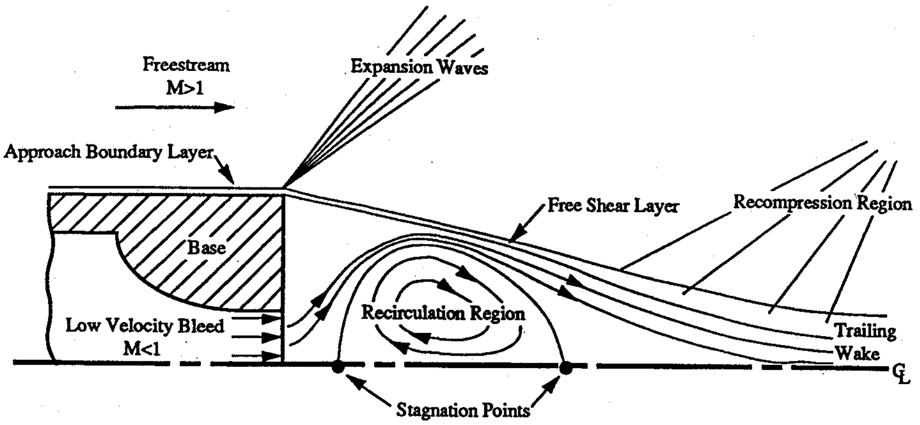

Fig. 1 Schematic of the near-wake flowfield with base bleed.

including the freestream Mach number, the size and geometry of the bleed orifice, and the flow rate, molecular weight, and temperature of the bleed gas. Increases in base pressure ratio (relative to the no-bleed case) from 10 to 90% have been reported for various combinations of the aforementioned parameters. As the bleed rate is increased past the optimum value, the base pressure ratio decreases (regime 2) until it reaches a relative minimum. A further increase in the bleed flow leads to the onset of power-on conditions (regime 3) when the bleed flow becomes supersonic, resulting in an increase in base pressure ratio.

From the combined results of the above experiments, base-bleed effectiveness is seen to increase with freestream Mach number, i.e., at higher Mach numbers, the peak base pressure occurs at lower I, and the percentage increase in base pressure is also higher. The effects of the bleed jet exit area on base pressure have also been investigated.[3,4,6–8] At very low bleed rates, the increase in base pressure with bleed is nearly independent of the area ratio; however, at higher bleed rates, the effectiveness of base bleed was shown to be improved by larger jet-to-base diameter ratios. Injection with porous bases is found to be the most effective.[7]

Experiments using air, hydrogen, helium, argon, and nitrogen have shown that base bleed is more effective when a bleed gas with lower molecular weight (relative to the freestream gas) is used.[8,9] The peak base pressure is higher, and occurs at a lower value of I with a lighter bleed gas. Significant increases in base pressure have also been observed using a heated bleed gas.[10] At low injection rates, the base pressure rise is nearly proportional to the enthalpy of the bleed gas. The peak base pressure is higher, and occurs at a lower value of I, than for the corresponding cold bleed case. Base burning with hydrogen results in even higher base pressures than with hot bleed.[9] Base bleed with fuel-rich solid combustion[11] has been shown to be even more effective. The advantage of combustion and burning over hot gas injection is suspected to be due to the different mechanisms and locations of enthalpy release in the wake. Investigation of the combined effects of boattailing and base bleed[12] showed that although the two effects were additive, there was a very weak dependence of optimum boattail angle on bleed rate, and of optimum bleed rate on boattail angle.

While the effectiveness of base bleed as a drag-reducing technique is well known, the details of the fluid-dynamic interactions caused by base bleed are not clearly understood. Most of the above experimental investigations were carried out prior to the development of reliable nonintrusive diagnostic methods, and their scope was primarily limited to determining the global influence of various base-bleed parameters on base pressure. Some results from earlier studies are also unreliable due to possible interference arising from model support effects[3,6] or nozzle flow nonuniformity. In addition, the results of some of the previous investigations of base bleed have been confounded by the added influences of boattailing, hot gas injection, and/or base burning. A clear understanding of the base-bleed phenomenon is hampered by a lack of detailed flowfield data.

Analytical models based on an empirical component-type approach[13] provide some insight into the physical processes that might be associated with base bleed. Although these models can only represent the base-bleed flowfield in a time-mean sense, and cannot account for its instantaneous turbulent nature, they have been fairly successful in predicting the qualitative effects of base bleed on base pressure.[14–17] Base-bleed computations[18–22] using the Reynolds-averaged Navier–Stokes equations have also been successful in predicting qualitative base pressure trends and in capturing flowfield structure details. Numerical techniques are currently limited by turbulence modeling issues, insufficient grid resolution, and lack of detailed experimental data for validation.[23]

Recent experimental efforts have provided insight into the complex interactions prevalent in the near-wake flowfields of blunt-based[1] and boattailed[2] afterbodies; however, no known detailed measurements of the base-bleed flowfield have been made to date. The objectives of the present research are to investigate the effects of base bleed on the near-wake flowfield of a cylindrical afterbody in supersonic flow, and to identify the dominant fluid-dynamic mechanisms inherent in this complex flow with the aid of laser-based optical diagnostic techniques. The measurements obtained provide a set of benchmark baseline data that will enhance the overall understanding of base flow phenomena and also serve to validate modeling and computational efforts in this field.

Experimental Facilities and Equipment

Figure 2 is a schematic of the supersonic, blowdown-type wind tunnel at the University of Illinois Gas Dynamics Laboratory designed solely for the study of axisymmetric base flows. High-pressure air from a tank farm enters the top of the stagnation chamber and passes through a screen–honeycomb–screen flow-conditioning module. The air is expanded to a design Mach number of 2.5 in the test section using a converging–diverging nozzle. The pressure and temperature in the stagnation chamber are 471 ± 3.5 kPa and 300 ± 2 K, respectively, for these experiments. Two square glass side windows provide optical access to the flowfield. The air in the test section exits through a conical diffuser and exhaust duct to the atmosphere. The afterbody is mounted at the end of a hollow sting, which is supported at two axial locations upstream of the nozzle to avoid support disturbances in the flowfield. A detailed description of the wind-tunnel design is provided in Ref. 24.

For the purposes of the base-bleed study, several additions were made to the existing wind tunnel. A stainless steel bleed line was designed and constructed with 50.8-mm-diam pipe sections to facilitate conditioning, measurement, and control of the bleed flow. Since the base pressure is significantly subatmospheric, ambient room air at 293 ± 2 K is an adequate source for the bleed air supply. The inlet consists of a screen followed by an elliptically rounded intake section to condition the incoming bleed flow. This is followed by about 1.3 m of pipe to ensure adequate flow development prior to the mass flowmeter. The electronic flowmeter consists of a temperature and a velocity probe and works on the hot-wire principle. The linearized output is directly proportional to the actual mass flow rate, and is unaffected by pressure and temperature fluctuations in

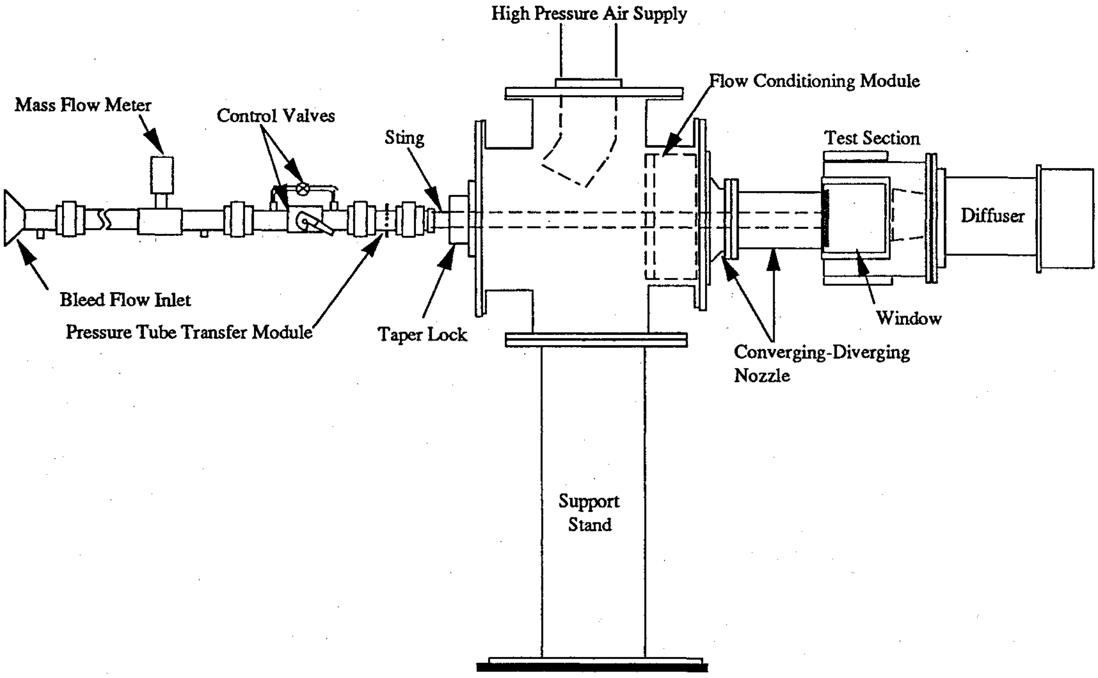

Fig. 2 Axisymmetric wind-tunnel and base-bleed facility.

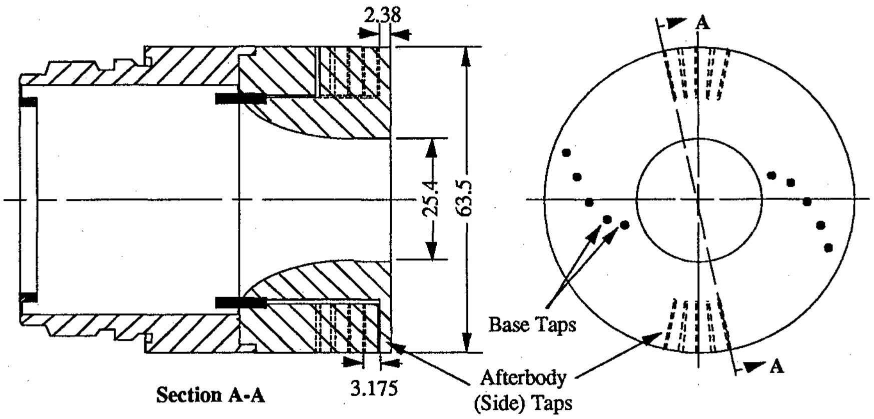

Base taps: 3.175 mm radial separation
Side taps: 3.175 mm axial separation
Bleed hole area = 16% of base area

All dimensions are in mm

Fig. 3 Location of static pressure taps on base-bleed afterbody.

the supply air. The flowmeter is followed by a butterball valve for coarse bleed flow control mounted in parallel with a needle valve for fine control.

A schematic of the afterbody used in the base-bleed studies is shown in Fig. 3. The 63.5-mm-diam cylindrical afterbody contains a 0.4 caliber bleed orifice, which is preceded by an elliptically contoured section based on ASME long-radius nozzle standards[25] to ensure a uniform velocity profile for the bleed flow exiting the base. Ten 0.635-mm-diam static pressure taps on the base plane are used to measure the radial distribution of the base pressure. Two sets of five taps each along the sting side surface, located diametrically opposite to each other, are used to measure the approach pressure distribution upstream of the base. The taps in each set are staggered along the periphery to prevent interference waves from the upstream taps affecting the measurements of the taps downstream. Static pressure measurements are obtained using a digital pressure transmitter controlled by a desktop computer via a serial interface. A removable retaining ring confines the pressure tubing near the inner wall of the afterbody in the region upstream of the bleed exit orifice to minimize disturbances in the bleed flow.

The two-component laser Doppler velocimetry (LDV) system used for this investigation uses the green (514.5 nm) and blue (488 nm) lines of a 5-W argon-ion laser. The nominal blue and green fringe spacings are 10.3 and 11.3 μm, respectively. The measurement volume diameter is 120 μm. Upstream frequency shifting of 40 MHz is used to discriminate flow direction and reduce fringe biasing, and the beam pairs are oriented at ±45 deg to the mean-flow direction to minimize fringe blindness. The receiving optics collect light scattered by particles crossing the measurement volume in 20-deg-off-axis forward scatter mode (effective length of measurement volume 730 μm). The scattered light intensity is converted to an analog voltage signal by photomultiplier tubes and fed to a digital burst correlator to extract frequency, and hence, velocity information. Three sets of stepper motors, encoders, and drives operate in a closed loop with a desktop computer to provide translation of the optical table in all three directions. A six-jet atomizer containing 50-cP silicone oil provides seed particles (nominal diameter 0.8 μm) to four seed tubes through a manifold and system of regulating valves. Three seed tubes for the freestream flow, arranged 120 deg apart circumferentially, are located just downstream of the flow-conditioning module. The seed tube for the bleed flow is located in the bleed line, just downstream of the butterball valve. A detailed description of the LDV system, including an error analysis, has been provided in Ref. 24. The worst-case rms error due to particle lag just downstream of separation has been estimated at 6%. This error is 1.7% one base radius downstream of the base plane, and continues to diminish further downstream. The estimated worst-case uncertainty is 1.2% of U_1 in the mean velocity, and 2.3% of U_1 in the rms velocity fluctuation measurements.

Results and Discussion

Pressure Measurements

Static pressure distributions along the afterbody and on the base plane were obtained for ten bleed rates ranging from $I = 0$ to $I = 0.032$. The axial pressure distribution of the approach flow along the afterbody was independent of the bleed rate. The approach static pressure was also nearly constant in the streamwise direction at $P/P_0 = 0.061 \pm 0.001$, yielding an isentropic Mach number of 2.47. A slight rise in pressure approaching the base corner was consistent on both sets of diametrically opposed pressure taps, and was most probably due to weak waves originating at the wind-tunnel nozzle throat interacting with the boundary layer on the sting near the base plane.

The radial distribution of base pressure ratio is shown in Fig. 4 for all ten bleed flowrates. At any given bleed rate, the base pressure ratio profile is radially symmetric across the base annulus and fairly independent of radial location, except for a slight increase near the base corner in some cases. This slight increase in base pressure is probably due to the sharp change in flow direction during entrainment of the low-speed flow by the high-speed shear layer near the base corner. It is also evident that the base pressure ratio initially increases with bleed rate (solid-symbol cases), peaks at around $I = 0.0148$, and then decreases rapidly as the bleed rate is increased further (open-symbol cases). This behavior is more clearly seen when the average base pressure ratio, based on the area-weighted average of each profile, is plotted as a function of the injection parameter (Fig. 5). Data from the blunt base and the 5-deg boattailed afterbody results[1,2] are also presented in this plot. The peak average base pressure ratio of $P_b/P_1 = 0.669$ at $I = 0.0148$ is 18.5% higher than the average base pressure ratio of the blunt-based cylinder and 5.7% higher than that of the boattailed afterbody. The difference in the average base pressure ratio between the blunt base[1] and the $I = 0$ no-bleed case is discussed later.

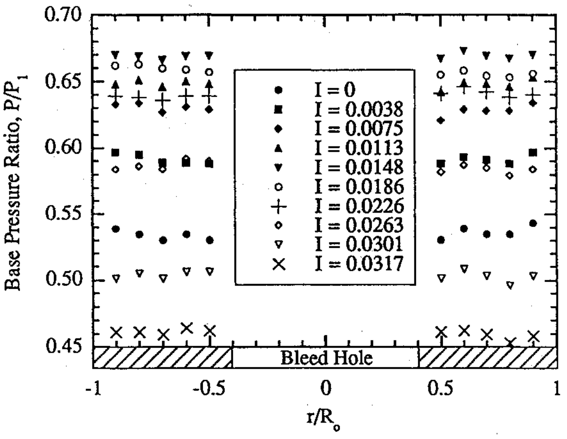

Fig. 4 Effect of base bleed on base pressure distribution.

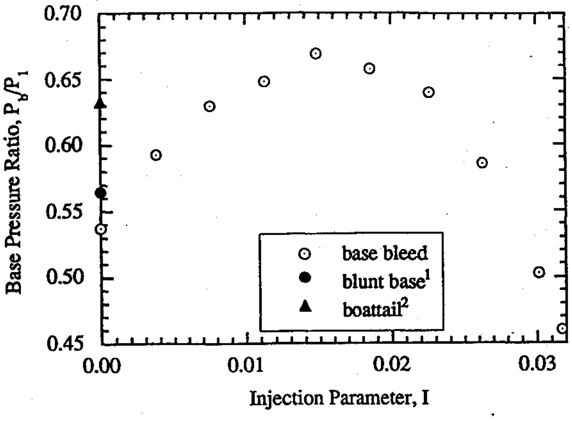

Fig. 5 Effect of base bleed on area-averaged base pressure ratio.

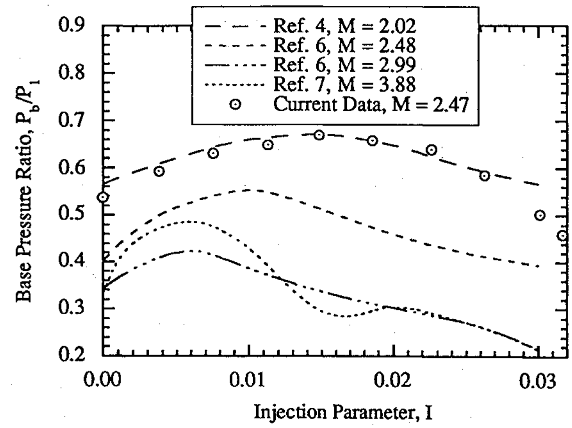

Fig. 6 Comparison of base-bleed results with other experiments (bleed orifice diameter ratio $d_j/d_b = 0.4$).

As seen in Fig. 6, the peak in the average base pressure ratio at $I = 0.0148$ is consistent with earlier experiments.[4,6,7] All of these data were obtained with bleed orifices of 0.4 caliber. There are, however, significant differences in the magnitudes of the base pressure curves. In spite of operating at nearly the same Mach number, the base pressure ratios of Ref. 6 are noticeably lower than those of the current study, possibly because of interference from the struts that were used to support their model. On the other hand, data[4] at Mach 2 are very similar to the current data. The difference in the bleed nozzle contours used in the two models could be responsible for the similarity of these data sets at different Mach numbers. The model used in the current study (and by Ref. 7) employs a contoured converging nozzle, whereas the orifice used in Ref. 4 was preceded by a 5-deg conical Mach 2.0 nozzle, similar to the one used in the study of Ref. 6. In addition, a thick boundary layer has a base-pressure-enhancing effect similar to that of base bleed. Differences in the approach boundary-layer thicknesses of the different experiments could therefore also contribute to the discrepancies discussed above. Although the second peak in base pressure in Ref. 7 is attributed to the converging nozzle preceding the bleed orifice, no secondary peak was observed in the current investigation. In view of the lower Mach number used in the present study, it is possible that the secondary peak could occur at a bleed rate higher than the range of the flowmeter.

Flow Visualization

Spark–schlieren photographs and shadowgraphs, obtained with a standard Z-type two-mirror configuration and a 1.4-μs micropulser light source, were used to confirm interference-free operation and to obtain qualitative information on the effect of base bleed on the near-wake flowfield. Schlieren photographs using a horizontal knife-edge at five different bleed rates are shown in Fig. 7. The absence of any strong interference waves emanating from the nozzle-exit/test-section junction confirms interference-free flow conditions in the test section at all of these bleed flow rates. At zero bleed, a strong recompression shock system is evident near the rear stagnation point. As expected, the shear-layer angle becomes flatter, the base corner expansion weakens, the wake widens, and the recompression shocks become weaker as the bleed flow rate is increased from zero to $I = 0.0033$. The recompression shock system seems to weaken considerably near $I = 0.0131$, when the bleed flow presumably provides most of the fluid required for shear-layer entrainment. As the bleed rate is increased further to $I = 0.0199$, the recompression shock system reappears slightly upstream of its earlier location. When the bleed exit velocity approaches sonic conditions at around $I = 0.0279$, the Mach disk emanating from the bleed orifice interacts with the oblique recompression shocks from the outer flow and forms a fairly complex shock system. This shock system also

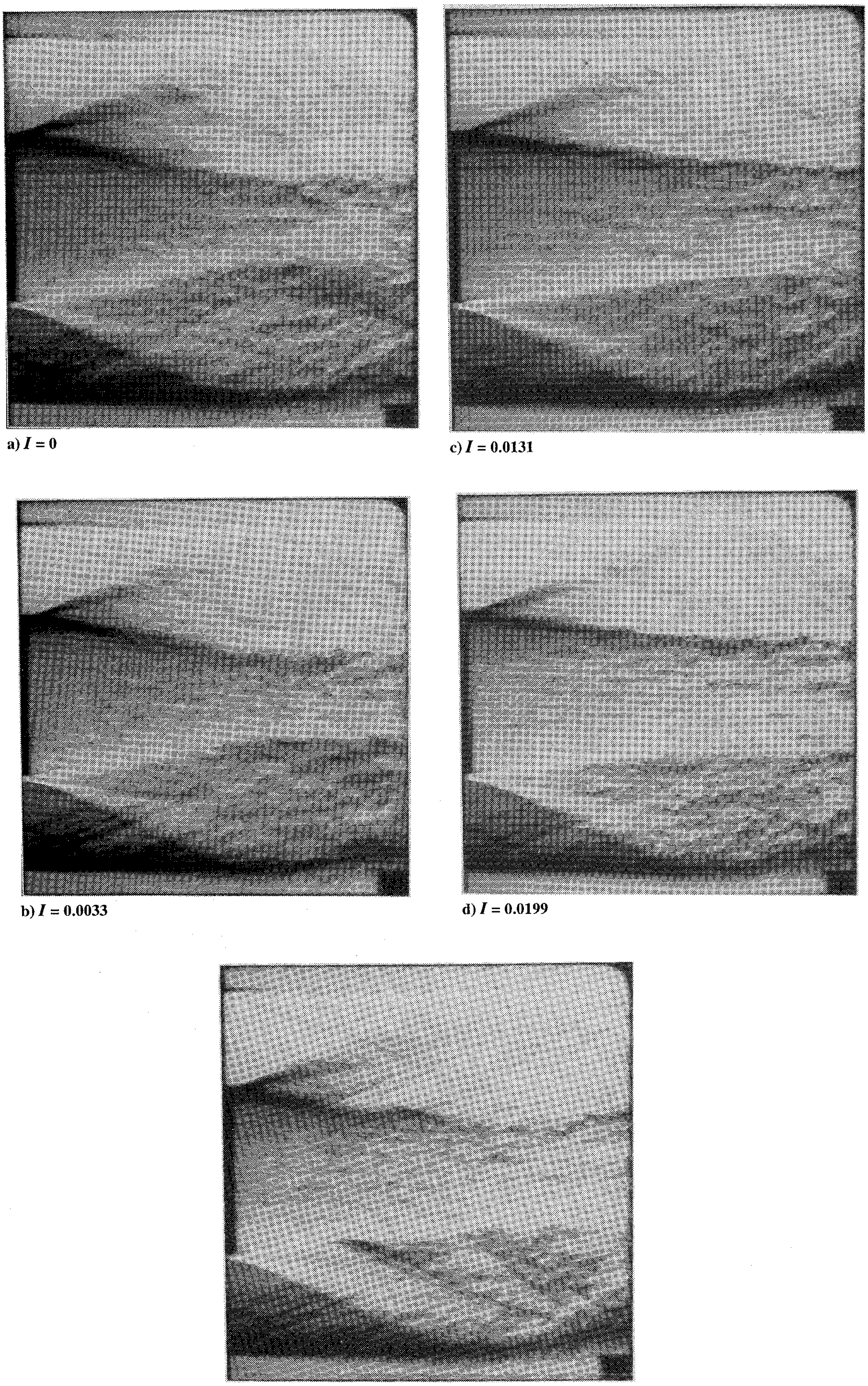

a) $I = 0$

c) $I = 0.0131$

b) $I = 0.0033$

d) $I = 0.0199$

e) $I = 0.0279$

Fig. 7 Schlieren photographs of the base flowfield at different bleed flow rates.

appears to be highly unsteady, as indicated by imaging the flowfield on a screen and by visual inspection of a series of photographs at this bleed rate. The horizontal knife-edge makes it difficult to discern the vertical Mach disk in the schlieren photographs; however, it is clearly visible in shadowgraphs taken at the high bleed rate. The axisymmetric nature of the flow also causes smearing of the flow features due to line-of-sight integration effects.

A parametric study of the mean axial velocity and turbulence quantities along the centerline has been performed using LDV. The approach flowfield and boundary layer and the flow conditions at the exit of the bleed jet have also been documented for the five bleed cases studied. Care was taken to match data rates at the freestream and bleed flow nozzle exits, in an effort to minimize particle concentration bias errors. Post-facto corrections for velocity bias were made using the interarrival time weighting method, which has been shown[26] to be the most reliable technique for high-speed separated flows.

The freestream approach flow was found to be uniform and independent of the bleed rate. The mean freestream approach velocity was found to be 574 m/s with 0.3% variation between the different bleed cases. The mean Mach number based on adiabatic expansion from the tunnel stagnation temperature to the freestream velocity was 2.45, in close agreement with the isentropic value of 2.47 based on pressure measurements. The unit Reynolds number was calculated to be 45×10^6 m^{-1} at the nozzle exit. Approach boundary-layer mean velocity profiles for all bleed cases were similar, as seen in Fig. 8. Curve fits[27] of these profiles were used to determine boundary-layer parameters such as integral thicknesses and skin-friction coefficient. These results (mean values and percentage variations over the five bleed cases) are presented in Table 1. The thicknesses and the friction velocity have been normalized by the afterbody radius and the freestream velocity, respectively. Rather large variations in the computed parameters (between the different bleed cases) are due to the sensitivity of the curve fit to accurate y-position determination (limited to ±0.1 mm due to hysteresis of the traverse table). The axial turbulence intensity and Reynolds shear stress distributions in the boundary layer collapse very well for the different bleed rates, as seen in Figs. 9 and 10. As expected, the magnitudes of these quantities are high in the boundary layer, dropping rapidly to low values in the freestream.

Table 1 Approach boundary-layer properties

δ/R_0	$0.102 \pm 1.6\%$
δ^*/R_0	$0.0241 \pm 6.8\%$
θ/R_0	$0.00682 \pm 6.0\%$
H	$3.53 \pm 1.1\%$
Π	$0.768 \pm 17\%$
C_f	$0.00170 \pm 4.7\%$
u_τ/U_1	$0.0414 \pm 2.3\%$

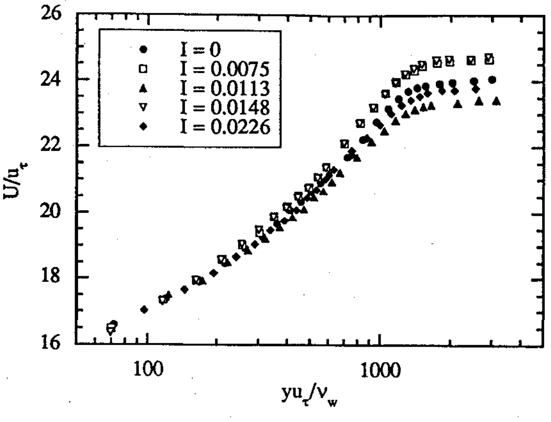

Fig. 8 Approach boundary-layer mean velocity profiles ($x/R_0 = -0.157$).

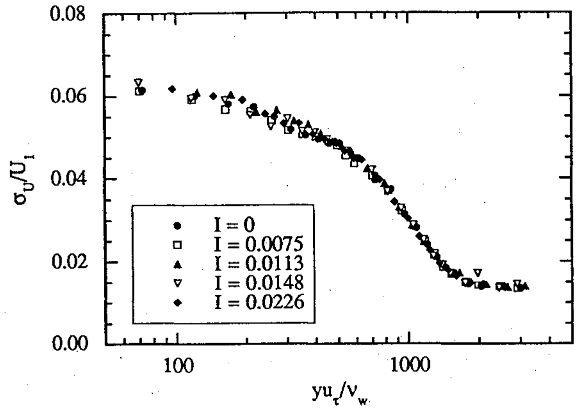

Fig. 9 Streamwise turbulence intensity distributions in approach boundary layer.

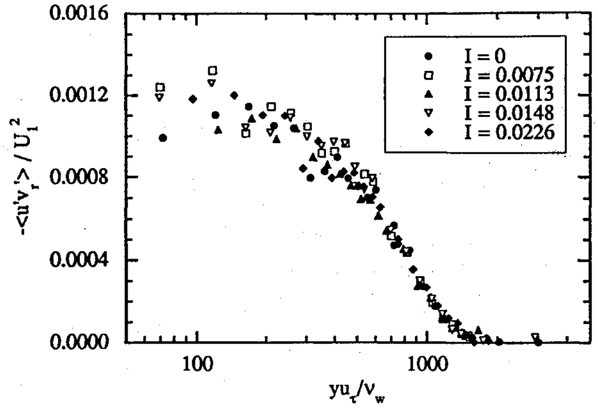

Fig. 10 Reynolds shear stress distributions in approach boundary layer.

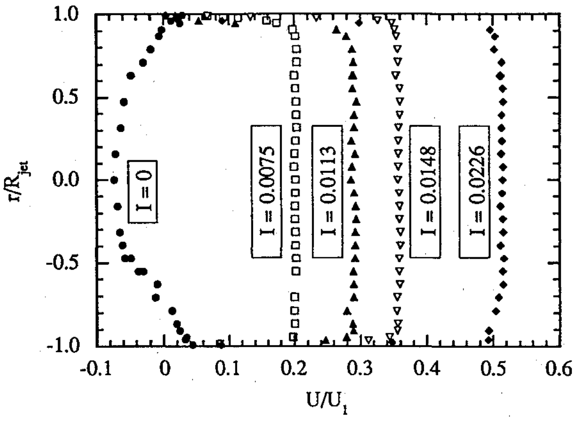

Fig. 11 Mean axial velocity distributions at bleed orifice exit ($x/R_{\mathrm{jet}} = 0.118$; $R_{\mathrm{jet}}/R_0 = 0.4$).

Radial traverses performed 1.5 mm downstream of the bleed exit plane show uniform velocity distributions in the bleed flow, as seen in Fig. 11. The effect of the compliant (open) boundary presented by the bleed hole can be seen for the bleed-off case. There is a mean inflow into the base along the centerline, and a mean outflow along the periphery of the bleed orifice. Bimodal velocity histograms were observed at all radial locations for the no-bleed case, indicating large-scale turbulence interaction between the recirculation region and the long passive cavity presented by the bleed hole and the hollow sting. The 5% difference in the average base pressure ratio between the blunt base[1] and the $I = 0$ case (Fig. 5) could be due to this compliant boundary effect.

The effect of base bleed on the mean axial velocity distribution along the centerline can be seen in Fig. 12. In all cases, the measured radial velocity component was less than 2% of U_1, and the Reynolds shear stresses were nearly zero, confirming that the LDV measurement volume was located at the centerline of the flowfield. For the no-bleed case, the peak reverse velocity (30% of U_1) and

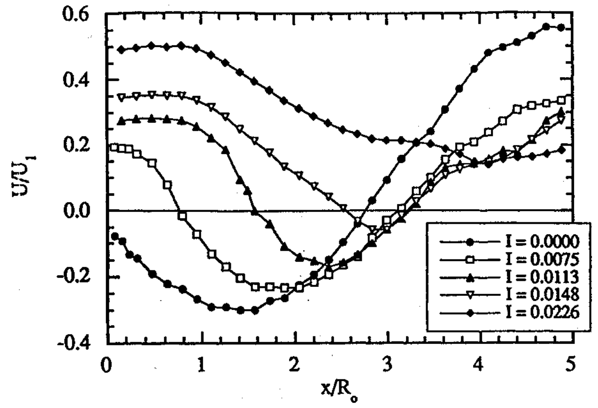

Fig. 12 Mean axial velocities along the centerline.

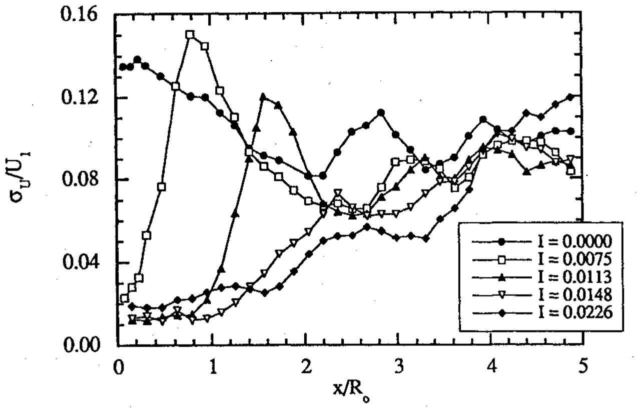

Fig. 13 Axial turbulence intensities along the centerline.

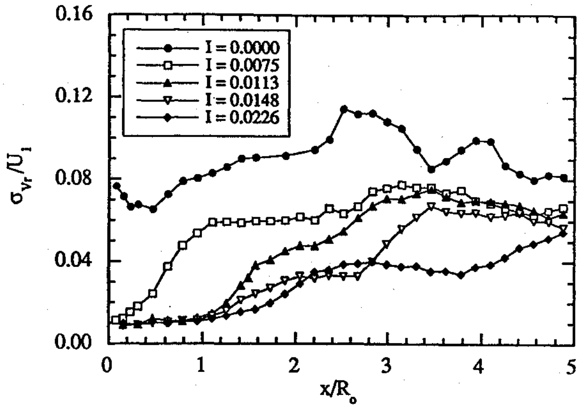

Fig. 14 Radial turbulence intensities along the centerline.

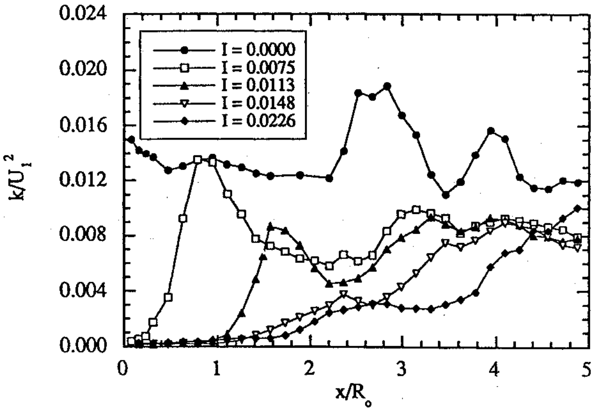

Fig. 15 Turbulent kinetic energy distributions along the centerline.

the rear stagnation point occur 1.5 and 2.8 base radii downstream of the base, respectively. These results are nearly identical to measurements done with a blunt base.[1] At the base plane ($x = 0$), however, the extrapolated axial velocity is nonzero and negative, due to the compliant-boundary effect discussed above. As the bleed rate is increased, the bleed jet exit velocity increases, causing a downstream shift of the forward stagnation point where the bleed flow and reverse flow meet. This downstream shift of the forward stagnation point with increasing bleed rate has the effect of diminishing the size of the recirculation region, since the rear stagnation point location is nearly constant at $x/R_0 = 3.2$ (note that this position for the bleed-on cases is shifted relative to the bleed-off case). The peak reverse velocity location occurs progressively downstream, and its magnitude decreases with increasing bleed. At $I = 0.0148$, the optimum bleed rate from a base pressure viewpoint, the recirculation region along the centerline almost disappears. No reverse velocity is detected along the centerline for the $I = 0.0226$ case, indicating penetration of the bleed jet into the reattachment zone. The velocity profiles for the bleed-on cases become similar for $x/R_0 > 3$, the wake redevelopment region.

Figures 13 and 14 present the axial and radial turbulence intensity distributions along the centerline. For each bleed case (except $I = 0.0226$), two peaks are observed in the distribution of turbulence intensity. The first peak occurs at the forward stagnation point because of the change in flow direction from axial to radial when the bleed flow meets the reverse flow in the recirculation region. The magnitude of this peak is seen to decrease with increasing bleed rate, because of the smaller influence of the diminishing recirculation region. The second peak occurs at the rear stagnation point due to reattachment phenomena. The influence of the flow mechanisms occurring at both stagnation points is much stronger in the axial direction. Consequently, the peaks in the radial turbulence intensity distributions are not as pronounced as the axial intensity peaks. At the higher bleed rates, the bleed flow penetrates further into the wake, accounting for the low centerline turbulence intensities seen in Figs. 13 and 14 for these cases. Anisotropy of the turbulent normal stress along the centerline is also evident from the differences in the axial and radial turbulence intensity profiles. Figure 15 shows the centerline distribution of turbulent kinetic energy, calculated using

$$k = 0.5\left(\sigma_U^2 + 2\sigma_{Vr}^2\right) \tag{1}$$

The occurrence of the peak energy magnitudes at the stagnation points, and likewise the decreasing energy levels with increasing bleed rate, are similar to those discussed for the turbulence intensity distributions.

Conclusions

An experimental investigation has been conducted to study the effects of base bleed on the near-wake flowfield of a cylindrical afterbody in supersonic flow. Data have been obtained using static pressure measurements, schlieren and shadowgraph photography, and LDV traverses along the centerline. Results indicate nearly uniform radial pressure profiles across the base plane. With increasing bleed flow rate, the average base pressure is found to increase initially, attain a peak value, and then decrease with further increase in the injection parameter, I. The approach flowfield upstream of separation is unaffected by the bleed rate. An increase in the bleed rate is accompanied by the diminishing size and intensity of the recirculation region (due to the downstream displacement of the forward stagnation point) and a decrease in the peak axial and radial turbulence intensities at the forward stagnation point. Near the optimum bleed rate of $I = 0.0148$, the base pressure is maximized, and the flowfield is characterized by the widening of the wake, flattening of the shear-layer angle, and the near-disappearance of reverse velocity along the centerline.

Acknowledgment

The authors gratefully acknowledge the financial support of the U.S. Army Research Office (Contract No. DAAH04-93-G-0226) with Thomas L. Doligalski serving as contract monitor.

References

[1] Herrin, J. L., and Dutton, J. C., "Supersonic Base Flow Experiments in the Near Wake of a Cylindrical Afterbody," *AIAA Journal*, Vol. 32, No. 1, 1994, pp. 77–83.

[2] Herrin, J. L., and Dutton, J. C., "Supersonic Near-Wake Afterbody Boattailing Effects on Axisymmetric Bodies," *Journal of Spacecraft and Rockets*, Vol. 31, No. 6, 1994, pp. 1021–1028.

[3] Cortright, E. M., and Schroeder, A. H., "Preliminary Investigation of Effectiveness of Base Bleed in Reducing Drag of Blunt-Base Bodies in Supersonic Stream," NACA RM E51A26, March 1951.

[4] Reid, J., and Hastings, R. C., "The Effect of a Central Jet on the Base Pressure of a Cylindrical Afterbody in a Supersonic Stream," Aeronautical Research Council (Great Britain), Reports and Memoranda No. 3224, Dec. 1959.

[5] Badrinarayanan, M. A., "An Experimental Investigation of Base Flows at Supersonic Speeds," *Journal of the Royal Aeronautical Society*, Vol. 65, 1961, pp. 475–482.

[6] Bowman, J. E., and Clayden, W. A., "Cylindrical Afterbodies in Supersonic Flow with Gas Ejection," *AIAA Journal*, Vol. 5, No. 6, 1967, pp. 1524, 1525.

[7] Valentine, D. T., and Przirembel, C. E. G., "Turbulent Axisymmetric Near-Wake at Mach Four with Base Injection," *AIAA Journal*, Vol. 8, No. 12, 1970, pp. 2279, 2280.

[8] Zakkay, V., and Sinha, R., "An Experimental Investigation of the Near Wake in an Axisymmetric Supersonic Flow with and without Base Injection," *Israel Journal of Technology*, Vol. 7, No. 1–2, 1969, pp. 43–53.

[9] Hubbartt, J. E., Strahle, W. C., and Neale, D. H., "Mach 3 Hydrogen External/Base Burning," *AIAA Journal*, Vol. 19, No. 6, 1981, pp. 745–749.

[10] Clayden, W. A., and Bowman, J. E., "Cylindrical Afterbodies at $M = 2$ with Hot Gas Ejection," *AIAA Journal*, Vol. 6, No. 12, 1968, pp. 2429–2431.

[11] Ding, Z., Chen, S., Liu, Y., Luo, R., and Li, J., "Wind Tunnel Study of Aerodynamic Characteristics of Base Combustion," *Journal of Propulsion and Power*, Vol. 8, No. 3, 1992, pp. 630–634.

[12] Bowman, J. E., and Clayden, W. A., "Boat-Tailed Afterbodies at $M = 2$ with Gas Ejection," *AIAA Journal*, Vol. 6, No. 10, 1968, pp. 2029, 2030.

[13] Korst, H. H., "A Theory for Base Pressures in Transonic and Supersonic Flows," *Journal of Applied Mechanics*, Vol. 23, No. 4, 1956, pp. 593–600.

[14] Korst, H. H., Page, R. H., and Childs, M. E., "A Theory for Base Pressures in Transonic and Supersonic Flow," Engineering Experiment Station, Mechanical Engineering Dept., Univ. of Illinois, ME TN 392-2, March 1955.

[15] Korst, H. H., Chow, W. L., and Zumwalt, G. W., "Research on Transonic and Supersonic Flow of a Real Fluid at Abrupt Increases in Cross Section (with Special Consideration of Base Drag Problems)," Engineering Experiment Station, Mechanical Engineering Dept., Univ. of Illinois, ME TR 392-5, Oct. 1964.

[16] Reijasse, P., Benay, R., Delery, J. M., and Lacau, R. G., "Missile and Projectile Base-Flow Prediction by Multi-Component Methods," AIAA TP 1988-90, Aug. 1988.

[17] Reijasse, P., Benay, R., Delery, J., and Lacau, R. G., "Prediction of Powered Missile or Projectile Base Flows by Multicomponent Methods," *La Recherche Aerospatiale*, Vol. 1989-4, 1989, pp. 15–32.

[18] Sahu, J., Nietubicz, C. J., and Steger, J. L., "Navier–Stokes Computations of Projectile Base Flow with and without Mass Injection," *AIAA Journal*, Vol. 23, No. 9, 1985, pp. 1348–1355.

[19] Sahu, J., "Supersonic Flow over Cylindrical Afterbodies with Base Bleed," AIAA Paper 86-0487, Jan. 1986.

[20] Danberg, J. E., and Nietubicz, C. J., "Predicted Flight Performance of Base Bleed Projectiles," AIAA Paper 90-2069, July 1990.

[21] Nietubicz, C. J., and Sahu, J., "Navier–Stokes Computations of Base Bleed Projectiles," *Base Bleed: First International Symposium on Special Topics in Chemical Propulsion*, edited by K. K. Kuo and J. N. Fleming, Hemisphere, New York, 1991, pp. 93–106.

[22] Nietubicz, C. J., and Gibeling, H. J., "Navier–Stokes Computations for a Reacting, M864 Base Bleed Projectile," AIAA Paper 93-0504, Jan. 1993.

[23] Dutton, J. C., Herrin, J. L., Molezzi, M. J., Mathur, T., and Smith, K. M., "Recent Progress on High-Speed Separated Base Flows," AIAA Paper 95-0472, Jan. 1995.

[24] Herrin, J. L., "An Experimental Investigation of Supersonic Axisymmetric Base Flow Including the Effects of Afterbody Boattailing," Ph.D. Thesis, Univ. of Illinois at Urbana–Champaign, Urbana, IL, July 1993.

[25] Bean, H. S. (ed.), *Fluid Meters—Their Theory and Application*, 6th ed., Report of the ASME Research Committee on Fluid Meters, American Society of Mechanical Engineers, 1971, pp. 216–220.

[26] Herrin, J. L., and Dutton, J. C., "An Investigation of LDV Velocity Bias Correction Techniques for High-Speed Separated Flows," *Experiments in Fluids*, Vol. 15, 1993, pp. 354–363.

[27] Sun, C. C., and Childs, M. E., "A Modified Wall Wake Velocity Profile for Turbulent Compressible Boundary Layers," *Journal of Aircraft*, Vol. 10, No. 6, 1973, pp. 381–383.

J. C. Adams
Associate Editor